Precision Engineering 63 (2020) 49–61

Contents lists available at ScienceDirect

Precision Engineering

journal homepage: http://www.elsevier.com/locate/precision

Error analysis to minimize cross-axis couplings in 6-DOF motion systems with a single moving part

Vu Huy Nguyen [a,*], Won-Jong Kim [b]

[a] Lawrence Berkeley National Laboratory, Berkeley, CA, 94720, USA
[b] Texas A&M University, College Station, TX, 77843, USA

ARTICLE INFO

Keywords:
Perturbation reduction
Cross-axis couplings
Nano-positioning
Magnetic levitation
6-DOF stages

ABSTRACT

In multi-axis motion control, cross-axis couplings cause error force and position disturbances in an axis when a desired motion is generated along another axis. Different from the parasitic errors that result from the imperfections of the mechanical bearings and reference surfaces, cross-axis perturbations are caused by errors that occur both statically (geometrical errors) and dynamically (in the transient responses) and are more prevalent in air-bearing and magnetic-levitation (maglev) stages. The parasitic errors are heavily dependent on the sizes of the stage's mechanical components, while the cross-axis perturbations depend significantly on the mover's speed and acceleration. For stages using permanent magnets (PMs) and Lorentz coils, the causes of off-axis forces include 1) errors in the coil turns' straightness, perpendicularity, and parallelism of the motor axes, and 2) errors in the local magnetizations and PMs' fringing effects. The purpose of this paper is to analyze the topologies of 6-degree-of-freedom (6-DOF) single-moving-part stages to minimize cross-axis couplings. The outcome is a stage configuration with reduced couplings and cross-axis perturbations. This is supported by experimental results performed on a newly developed 6-DOF maglev laser-interferometer stage. Its achieved root-mean-square (rms) positioning noise and minimum step size in *XY* are 3 nm and 10 nm, respectively. Its achieved resolution in out-of-plane rotations is 0.1 μrad. In addition to the analysis supported by these results, this paper introduces a new measure to represent cross-axis perturbations and to compare the effects of couplings in multi-axis positioning. This measure is entitled the cross-coupling quantity (CCQ) and calculated from the displacement of the stage in the axis of interest, the peak time of the response, and the peak-to-peak (p-p) error in the perturbed axis.

1. Introduction

In multi-axis positioning, single-moving-part stages are the ones that have only one moving part performing the motions in all the possible axes [1,2]. A key advantage of these stages compared with multiple-moving-part motion systems, such as gantry stages and articulated robotic arms, is the avoidance of cumulative position errors due to the mechanical tolerances and errors at the bearings and joints. For single-moving-part motion stages, the mechanical components include 1) a moving platen, 2) the base, 3) actuators, and 4) bearings. Given that each actuator or bearing of the stage is broken down to a mover and a stationary part, in a single-moving-part stage the movers of all the actuators and bearings are rigidly assembled to the single moving platen. In most cases, rotational motions, either in-plane (*XY*) or out-of-plane, are realized by two actuators generating parallel forces in opposite directions [1–4]. For multi-axis nano-precision stages with millimeter-order strokes in *XY*, Lorentz coils have been used due to the need for non-contact force generation, and their linear force model facilitates the real-time feedback control [1–4]. Common design configurations for 6-DOF single-moving-part stages are a square [3], cross [4], and triangle [1], as illustrated in Fig. 1. The movers can be either PMs (coils are in the base) or coils (PMs are in the base). Here, 1 is the base, 2 is the single moving platen, and 3 is the moving part of the actuators or magnetic bearings.

The precision stages' performance specifications include settling time for a given displacement and velocity, rms positioning noise, position resolution, position accuracy, maximum speed and acceleration, load capability, and parasitic errors—the position error in one axis when the stage performs a full-stroke motion in another axis. In stages with mechanical bearings, the friction induced by cross-coupling forces normal to the bearing surfaces is a disturbance that degrades the positioning performance. The efforts on minimizing the parasitic errors in

* Corresponding author.
E-mail addresses: vu_nguyen@ieee.org, vhn@lbl.gov (V.H. Nguyen).

https://doi.org/10.1016/j.precisioneng.2019.11.013
Received 11 December 2018; Received in revised form 24 October 2019; Accepted 11 November 2019
Available online 24 November 2019

multi-axis positioning, however, have been reported mainly for flexure structures [5–8]. With rapid developments in semiconductor manufacturing, additive manufacturing, and microscopy, the requirements of motion stages have constantly increased [9–14]. Together with the nanoscale precision and multi-DOF positioning capability, the required travel ranges for the above applications are exceeding the capability of flexure stages. With 6-DOF single-moving-part stages using magnetic or air bearings, the position error in one axis over the travel range of another axis depends not only on bearings and reference surfaces but also on the loads and control performance. Here, instead of the static parasitic errors, it is more relevant to consider the cross-axis perturbation, which is the position fluctuation of one axis (perturbed axis) when a desired motion is generated in another axis (primary axis). Results with cross-axis perturbations were reported in [1,4,15–17].

Within a short displacement range, the cross-axis perturbations depend on the transient-response characteristics of the motion in the primary axis and its dynamic couplings with the perturbed axes. The main cause of cross-axis perturbations is the off-axis error forces or torques. These errors result from the (static and dynamic) couplings between multiple actuators of the same stage. The causes for off-axis error forces include 1) geometrical errors (perpendicularity and parallelism between the actuators' axes, straightness of Lorentz coils' turns, etc.), 2) couplings between the axes due to the actuators' structure (PMs' fringing effect, coils' end effect, etc.), 3) errors in the coil currents, and 4) other errors including coil fill factor and PMs' remanence. In case there are two actuators that are supposed to produce two equal forces in the same direction, the errors from the current amplifiers result in a difference in these forces, and thereby, an error torque. In this paper an on-axis force error is defined as the difference between the actual force generated by a single actuator along its main axis and the desired force to be generated in that axis. The causes 3) and 4) mentioned above produce this error. An off-axis error force is the undesired force generated in another axis (due to the causes of 1) and 2) above) when an actuator produces a desired force in its main axis.

The cross-axis coupling between x and y, for example, is the correlation in which a motion of the mover in x (primary axis) induces some undesired fluctuations in y (perturbed axis). The cross-axis coupling herein encompasses the static coupling, which originates from the static geometric errors, and the dynamic coupling that appears dynamically. The cross-axis perturbation caused by the underlying coupling mentioned above is the position profile (displacement versus time) along the perturbed axis. When mentioning a cross-axis perturbation, it has to be accompanied by the characteristics of the primary axis' motion (displacement, and speed, acceleration, or settling time) to reflect the cause of the perturbation. Introducing the CCQ as in this paper is an effective way to incorporate the characteristics of both the cross-axis perturbation and the primary axis' motion into a single parameter that can be used to compare the coupling levels.

Although leading to position errors and possibly system instability, the off-axis error forces and dynamic couplings in nano-precision multi-axis positioning have not yet been extensively investigated. Conventional methods in reported works mainly discussed the static errors and couplings, in which the off-axis errors were due to 1) mechanical bearings' imperfections and 2) the structural properties of flexures. The static coupling is an intrinsic property of a motion system; it shows up even when the power and control are turned off. The dynamic couplings, on the other hand, are present in the transient responses. Generally the static parasitic errors are larger with a larger motion range. The cross-axis perturbations, on the other hand, are larger with a higher motion speed and acceleration. The static analysis using parasitic errors, therefore, is inadequate to study the cross-axis perturbations caused by the errors that occur both statically and dynamically. For air-bearing and maglev stages, the concept of parasitic errors needs to be augmented to handle the cross-axis perturbations in transient responses.

The focuses of most reported works in maglev-system design and testing were mainly on the modeling and control of certain structures [1–3,16–18]. Besides, why a design configuration was selected was usually not well justified. Maglev and air-bearing stages with a single moving part have been reported with the capability to perform 6-DOF motion control with high precision [1,2]. However, challenges still remain in dealing with the off-axis error forces affecting the control performance in multi-DOFs at the scales of nanometers and micro-radians. No method has been established to evaluate the effect of cross-axis couplings in multi-axis transient responses, and no measure has been proposed to standardize the comparisons of the cross-axis perturbations.

This paper presents an analysis to quantify the effects of cross-axis couplings and compare those effects between the design topologies of multi-axis stages. The actuator of interest in this case is of Lorentz-force type, which has been commonly used for 6-DOF single-moving-part stages with a long XY stroke [1–4,15,16,18]. With a 6-DOF single-moving-part stage broken into its basic units (each is a Lorentz-force actuator), a bounded off-axis error force is assumed for each actuator. The effect of cross-axis couplings in the system model used for feedback control is quantified by the norm of the transformation matrix between the closed-loop control efforts and the coil currents. In Fig. 1, the actuator units of the three stages are assumed to have the same size and force-generation capability. Each actuator generates two orthogonal forces, one in the horizontal and the other in the vertical direction. The distance from the horizontal axis of symmetry of each actuator to the central vertical axis of the entire moving part, about which the torque is calculated, is the same, l. The off-axis error-force bounds of all the actuators are assumed to be the same. The question of interest is which design in Fig. 1 has the least cross-axis coupling. To answer this we establish a correlation between the bounded errors at the individual actuators and the variation ranges of the coil currents computed from the closed-loop control efforts. This in turn maps the magnitude of the bounded errors at the individual actuators to the variations of the applied forces needed for closed-loop control. Such a method, unattempted yet in the literature, allows for the topological analysis to tell which design configuration is best suited for a particular application.

Key contributions of this paper include 1) a multidisciplinary analysis on the sources of errors in multi-axis positioning, and 2) a method for quantitatively studying the effects of cross-axis couplings on the dynamics of single-moving-part stages. The topological analysis

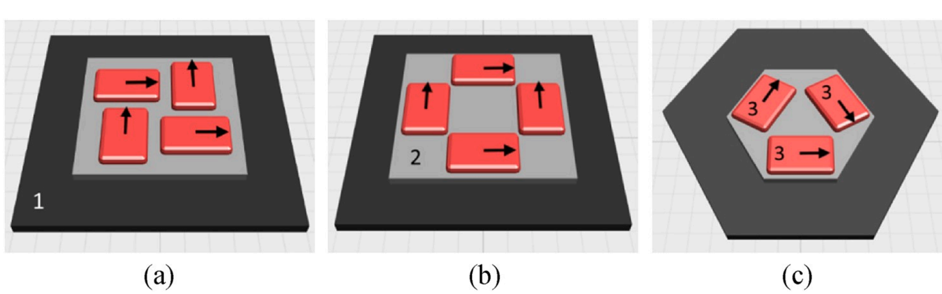

Fig. 1. The three configurations for single-moving-part stages, a) square, b) cross, and c) triangle.

presented herein helps evaluate the degrees of cross-axis couplings produced by the errors at the individual actuators in three stage configurations—triangular, cross, and square. This analysis is supported by a) experimental results from a 6-DOF maglev stage with a nanoscale and sub-micro-radian precision, and b) the comparisons between our stage's performances and those from existing works. In addition to these contributions, this paper establishes a measure for the performance comparisons between multi-axis stages. For the same step size in the primary axis, a higher speed and acceleration lead to larger perturbations in other axes. Therefore, to represent the couplings in multi-axis positioning, we incorporate the peak time of the step response and the ratio between the perturbed axis's p-p fluctuation and the primary axis' step size into a measure named the CCQ. Our experimental results with CCQ values are provided as a benchmark. Fig. 2 is a photograph of the experimental setup. The stage's travel range in *XY* with a nanoscale positioning resolution is 56 mm × 35 mm, limited by the size of the precision mirrors attached to the platen. The travel ranges in the vertical axis, rotations about the vertical axis, and out-of-plane rotations are, respectively, 40 μm, 3.72 mrad, and 0.52 mrad.

Section 2 of this paper discusses the design considerations for 6-DOF maglev stages with a nanoscale precision. Section 3 provides the analysis of stage configurations to determine how the cross-axis couplings introduce errors into the system dynamics. Section 4 presents experimental results to support the findings in Section 3. The conclusions are given in Section 5.

2. Design considerations for 6-DOF stages with long strokes in *XY*

2.1. Noise, force density, and moving Part's mass

In Ref. [19], Gu and Kim provided a detailed analysis on the quantification of the noise contributions from various sources including ground vibration, electronics noise, and the quantification noises from analog-to-digital converters (ADCs) and digital-to-analog converters (DACs). A noise propagation model was used to predict the noise level at various crossover frequencies and select the optimal control bandwidth [19]. In control system design, the effect of sensing noise on control performance leading to the selection of low-pass-filter corner frequencies, sampling rates, and closed-loop control bandwidths has been thoroughly studied [20–22]. With the same sensing noise and load, actuators with a higher force density need a lower loop-gain magnitude, resulting in a lower control bandwidth and output noise. For maglev stages with the same sensing noise and force-generation capability, the moving part with a smaller mass requires a smaller loop-gain magnitude to levitate the mover, and therefore leaves a larger amount of force to accelerate it in the lateral directions.

2.2. Magnet structures

For multi-axis stages with a single moving part, spatially periodic planar magnet arrays or matrices and Lorentz coils could allocate the forces in 6 DOFs [4,15]. With flexures, one could only realize up to 3-DOF motions with long travel ranges in *xy* [6–8]. A linear or planar magnet array is a PM structure with the magnets' magnetization directions periodically repeated in one dimension, usually along the structure's length [23]. At a certain point close to the array's surface and sufficiently far from its edges, there are two magnetic flux-density components, one normal to the array's surface, and the other along its length. Illustrated in Fig. 3 is a linear Halbach array, which strengthens the fundamental component of the magnetic flux-density in one side (positive-*z*) and cancels that in the other side of the structure. Halbach arrays are highly applicable in electric machines with a precise force model and a high force density [23]. A planar magnet matrix is a structure with the magnetization directions periodically repeated over two dimensions [15]. At a point close to the magnet matrix's surface, there are three magnetic flux-density components. In Refs. [15,24], only one planar magnet matrix was used with Lorentz coils for multi-axis long-stroke planar positioning with a single moving part. The magnet matrix as used in Refs. [15,24] was a superimposition of two single-axis linear Halbach arrays, one in *x* and the other in *y*.

2.3. The stage as a group of actuators, each produces two force components

In the open space near a magnet array as mentioned in Section 2.2, with two spatially periodic flux-density components, there must be two orthogonal forces generated by a current in a planar coil, one normal to the magnet array's surface and the other in the lateral direction. For a single coil, these forces are coupled and position-dependent. To make the normal and lateral forces independent, at least two coils must be grouped and energized simultaneously. Dividing the total number of coils of the actuation system into spatially separated groups helps 1) allocate certain groups of coils to the actuation along each axis, and 2) allow for the multi-DOF system modeling with the torques calculated from the distances between the geometrical centers of the groups and the symmetry axis of the entire moving part. Splitting into groups of coils, each generating two independent forces, also facilitates the control design and implementation.

A group of coils working with the associated magnet array as mentioned above is named a forcer, a single actuator, or motor. In Ref. [15], the 6-axis stage consisted of three motors with three groups of coils attached to the moving platen; each group had 12 Lorentz coils. In Ref. [4], the 6-DOF stage was actuated by four motors with four linear Halbach arrays fixed to the moving part; each magnet array contained 12 magnet bars. To reduce modeling errors, each group of coils or a magnet array on the moving part must be sufficiently compact in the horizontal directions. This helps reduce the position variation of the equivalent Lorentz force's acting point. To facilitate the theoretical decoupling of the 6 control axes, the groups of planar coils or magnets on the moving part must be sufficiently separated. However, if they are relatively far from each other, the large size of the moving part makes it either heavier or less structurally rigid.

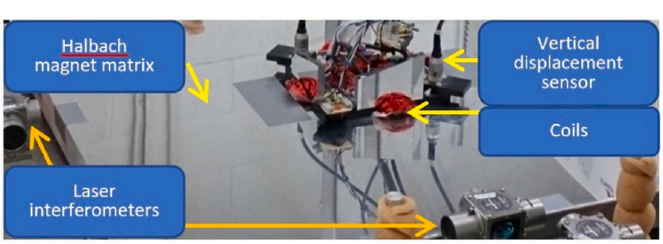

Fig. 2. Photograph of the 6-DOF maglev stage to support the analysis in this work.

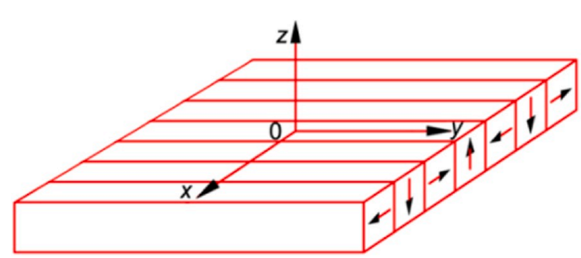

Fig. 3. Illustration of a linear Halbach array with the flux density components in *x* and *z*.

2.4. Error from the power amplifier circuits

A current amplifier unit contains a power operational amplifier (Op Amp) and at least one small-signal Op Amp for signal conditioning. Its input is the DAC signal commanded by the processing unit where the control routine is executed, and its output is the coil current. The amplifier itself adds noise and nonlinearity to the output currents, and, therefore, the motion system's dynamics. With a sufficiently high bandwidth of the amplifier, its dynamics is significantly faster than that of the motion stages and can be neglected in control design. However, the cost to pay for a higher bandwidth is a lower gain, leading to a larger input voltage swing. With the same DAC bit length, a larger voltage swing worsens the minimum incremental current generated by the amplifier.

On top of the noise introduced by the DC power supply, there are errors of the power amplifiers, including constant DC drifts, nonlinearities, and errors associated with the variations of electronic components' properties. Calibration can be done to compensate for or to eliminate the DC drifts. The other errors, however, cannot be avoided. At the milliampere scale, these errors introduce input uncertainties into the control system, limiting the positioning performance at the nanoscale. Table 1 lists the desired currents, measured currents' standard deviation (std), and p-p errors generated by 8 Lorentz coils, each with 0.19-Ω resistance and 59-μH inductance. The power Op Amp used herein is the APEX PA12A. The tolerance of the resistors in the power amplifiers is 1%. There is a closed-loop circuit to ensure that the desired output current is independent of the load characteristics at low frequencies. Table 1's data show that the amplifiers to provide the control inputs for the system are a significant source of error. Adding more coils and using a larger number of amplifiers, therefore, introduce more noises and errors to the system.

2.5. Coil ends and straightness

In long XY-stroke motion systems with planar magnet arrays and Lorentz coils, where the surfaces of coils and PMs are placed in parallel and close to each other to generate thrust or levitating forces, the shorter or narrower one among the two introduces its end effects to the system dynamics. In moving-magnet designs [2,18], where the PMs move in a space covered by the stationary coil arrays, their end effects present. In the stages with Lorentz coils moving on top of a larger magnet matrix [15,24], the coil ends' effects are present. In both cases, model uncertainties and force disturbances are introduced to the system dynamics.

Practically, long magnets or coils are desired so that the coil end or PM's fringing effects can be relatively small compared to the forces generated by the PM's or coil's main volume. For short coils the ratio between the end volume and total coil volume can be up to 43% [4]. Although the forces generated by the coil ends intersecting with a Halbach array could be quantified, these added nonlinearities into the system model, making it non-ideal for real-time feedback control. In addition, the wire turns curving around the corners made the coil sides not perfectly straight because the coil corners were not sufficiently far from each other. Below is an example where the straightness of the coil sides in Fig. 4(b) is significantly better than that in Fig. 4(a). This imperfection of the wire turn's straightness went into the system modeling error because the coils' sides were assumed to be ideally straight for the analytical Lorentz-force calculation.

One has to deal with either PM's fringing or coils' end effects in any design. The PMs' fringing effects depend heavily on their size, shape, and magnetization properties, of which the availability of the geometries and the variation of magnetic properties in individual parts are usually beyond the designers' control. In contrast, for Lorentz coils, the designers have full control of the coils' geometry and uniformity. Their shorter ends, which are not effective for force generation, can be bent away to be further from the PMs to minimize the undesired end effects.

Table 1
Desired electric currents and measured currents with a set of 8 coils.

Average desired current (mA)	4.29	12.62	107.74	213.40	424.80
std of measured currents (mA)	4.79	4.82	5.60	7.09	10.93
Ratio between std of measured and desired currents	**111.8%**	**38.2%**	**5.2%**	**3.3%**	**2.6%**
p-p of measured currents (mA)	14.49	14.46	14.90	19.20	30.20
Ratio between p-p of measured and desired currents	**338.0%**	**114.6%**	**13.8%**	**9.0%**	**7.1%**

2.6. Summary of design considerations

The discussions in this Section together with the data shown in Table 2 suggest that a reduced number of coils, a high force density, and a light moving part are needed for an ultraprecise stage. The multi-axis stages with a long XY-stroke and a single moving part consist of planar magnet arrays and Lorentz coil arrays, which are locally separated into forcers. Each forcer generates two independent and orthogonal forces. However, how to arrange the forcers in the moving platen to minimize cross-axis couplings still remains a question. This is addressed in Section 3.

3. Cross-axis coupling analysis

3.1. Qualitative analysis

For a triangular design as in Fig. 5 to generate a force in x, motor 2 needs to generate a force in x, F_{2x}, while motors 1 and 3 need to produce two opposite forces in y to balance the torque about the vertical axis generated by F_{2x} [15,24]. Totally three motors must be energized, and the currents in the motors 1 and 3 must be calculated based on F_{2x} so that the net torque about the vertical axis is ideally zero. In practice, due to the power amplifiers' nonlinearity and errors in the motor's geometry, errors are present. Feedback control helps reduce the effects of the errors on the positioning performance. However, for the achieved rms positioning noises on the order of nanometers and sub-microradians, minimizing the net errors of forces and torques must be planned early in the design phase. Considering each motor a source of bounded error, using

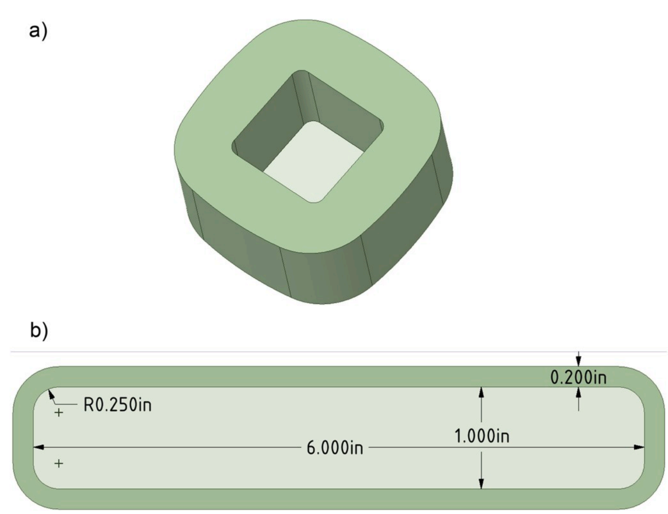

Fig. 4. 3-D rendering of the Lorentz coils used in 6-DOF maglev systems, (a) in Ref. [1], and (b) in Ref. [25].

Table 2
Coil numbers, platen weights, and the achieved rms positioning noises in reported works.

	Number of coils	Moving part's mass	RMS noise (closed-loop control)	Design configuration
Verma et al., 2006 [1],	6	0.27 kg	3 nm	Triangle, moving magnets
Hu and Kim, 2006 [15],	36	5.91 kg	8 nm	Triangle, moving coils
Zhu et al., 2016 [4],	60	Not reported	50 nm	Cross, moving magnets
Jansen et al., 2007 [18],	24/84	8.20 kg	100 nm	Square, moving magnets

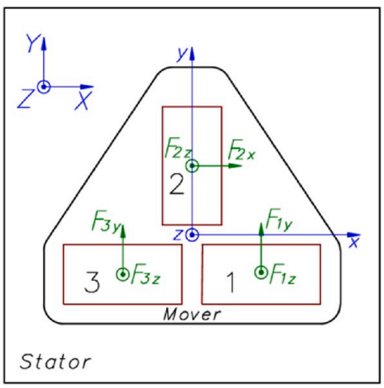

Fig. 5. Layout of a triangular-configuration planar-stage design [15,24].

two motors instead of three (to actuate the platen along a certain axis) reduces the net error.

For the square stage in Fig. 6, if a torque needs to be generated about the x-axis passing through the mover's geometric center, and, at the same time, a force needs to be produced in x, both two motors 1 and 3 must be energized. However, when motors 1 and 3 generate two forces in the opposite directions along z, they produce an undesired error torque about the y-axis. To cancel this error, motors 2 and 4 must be energized. Totally 4 motors must be energized in this case.

With the cross design as in Fig. 7, two motors 2 and 4, are sufficient to actuate the mover along the x-axis and, at the same time, generate an out-of-plane torque about this axis. For the square design in Fig. 6, the difference between F_{1z} and F_{3z} creates a toque about both x and y. For the cross layout in Fig. 7, the difference between the vertical forces F_{2z} and F_{4z} produces a desired toque about x. They, however, only generate a negligible error torque about y because the ideal acting points of the forces at motors 2 and 4 are aligned in the y-axis. In this case the width

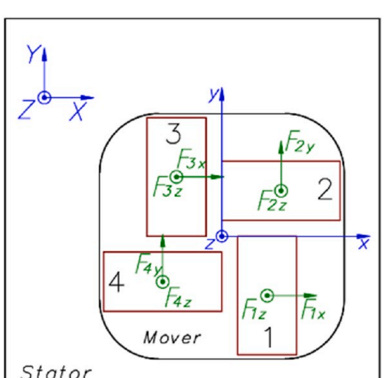

Fig. 6. Layout of a square-configuration planar stage design [3].

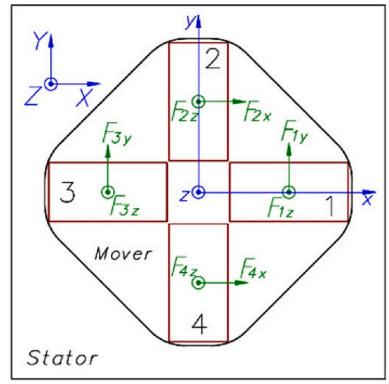

Fig. 7. Layout of a cross-configuration planar stage design.

along x of the actuators 2 and 4 must be properly designed so that the acting points of the equivalent z-axis forces are confined in a smallest possible distance to y.

Fig. 8 shows a triangular design with three forcers arranged in a Y shape [1]. Assuming that each forcer used for the designs in Figs. 5 and 8 generates the same maximum force, F_{max} in the XY plane, the maximum forces in x and y that the stage in Fig. 5 can produce are F_{max} and $2F_{max}$, respectively. These maximum forces, for the stage in Fig. 8 with $\alpha = \pi/6$ rad, are $2F_{max}$ and $\sqrt{3}F_{max}$.

3.2. Quantitative analysis

3.2.1. Analysis of cross-coupling in 6-DOF planar stages using Halbach arrays and Lorentz coils

In this analysis, $\boldsymbol{F_t}$ is the vector consisting of the total Lorentz forces and torques acting on the moving part of a 6-DOF stage as in Fig. 6–8. The design in Fig. 8, not Fig. 5, is selected to be compared with those in Figs. 6 and 7 because the Y-shape design in Fig. 8 is in symmetry, as with the square and cross designs, and the maximum forces it can produce in x and y are close, not far off as with the design in Fig. 5.

$$\boldsymbol{F_t} = \left[F_x\ F_y\ T_z\ T_x\ T_y\ F_z\right]^T \tag{1}$$

$\boldsymbol{F_a}$ is the vector consisting of the force components generated by the individual actuators that constitute the 6-DOF stage. With the square, cross, and triangular designs in Fig. 6–8, $\boldsymbol{F_a}$ is as follows, respectively.

$$\boldsymbol{F_{a\_square}} = \left[F_{1x}\ F_{1z}\ F_{2y}\ F_{2z}\ F_{3x}\ F_{3z}\ F_{4y}\ F_{4z}\right]^T \tag{2}$$

$$\boldsymbol{F_{a\_cross}} = \left[F_{1y}\ F_{1z}\ F_{2x}\ F_{2z}\ F_{3y}\ F_{3z}\ F_{4x}\ F_{4z}\right]^T \tag{3}$$

$$\boldsymbol{F_{a\_triangular}} = \left[F_{1h}\ F_{1z}\ F_{2h}\ F_{2z}\ F_{3h}\ F_{3z}\right]^T \tag{4}$$

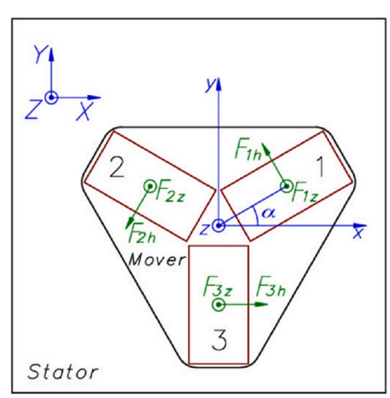

Fig. 8. Layout of a triangular planar stage design [1].

Here, F_{ju} is the Lorentz force component generated by the actuator numbered j along the u-axis. In case of the triangular design, F_{jh} is the Lorentz force produced by actuator j in the horizontal plane. The relation between $\boldsymbol{F_t}$ and $\boldsymbol{F_a}$ is

$$\boldsymbol{F}_t = \boldsymbol{A}\boldsymbol{F}_a. \tag{5}$$

Here, $\boldsymbol{A}$ is the constant-element matrix in Eqs. (6)–(8). Assumptions for this analysis are 1) the mover's center of mass is its geometric center in the XY plane, 2) each actuator generates two independent and orthogonal forces with the acting point at its geometric center seen in the XY plane, 3) the gap between the planar coils and the PMs' surface is constant, and 4) for all the actuators the distance to calculate the torque about the mover's vertical axis of symmetry is the same, l. This is to guarantee that an actuator can generate the same torque about the mover's vertical symmetric axis regardless of the design in which it is utilized. In Eq. (8), $\alpha = \pi/6$ rad for the design in Fig. 8 and $\alpha = 0$ for the one in Fig. 5.

$$\boldsymbol{A}_{square} = \begin{bmatrix} 1 & 0 & 0 & 0 & 1 & 0 & 0 & 0 \\ 0 & 0 & 1 & 0 & 0 & 0 & 1 & 0 \\ -l & 0 & -l & 0 & l & 0 & l & 0 \\ 0 & -l & 0 & l & 0 & l & 0 & -l \\ 0 & -l & 0 & -l & 0 & l & 0 & l \\ 0 & 1 & 0 & 1 & 0 & 1 & 0 & 1 \end{bmatrix} \tag{6}$$

$$\boldsymbol{A}_{cross} = \begin{bmatrix} 0 & 0 & 1 & 0 & 0 & 0 & 1 & 0 \\ 1 & 0 & 0 & 0 & 1 & 0 & 0 & 0 \\ l & 0 & -l & 0 & -l & 0 & l & 0 \\ 0 & 0 & 0 & l & 0 & 0 & 0 & -l \\ 0 & -l & 0 & 0 & 0 & l & 0 & 0 \\ 0 & 1 & 0 & 1 & 0 & 1 & 0 & 1 \end{bmatrix} \tag{7}$$

$$\boldsymbol{A}_{tr} = \begin{bmatrix} -\sin\alpha & 0 & -\sin\alpha & 0 & 1 & 0 \\ \cos\alpha & 0 & -\cos\alpha & 0 & 0 & 0 \\ l & 0 & l & 0 & l & 0 \\ 0 & l\sin\alpha & 0 & l\sin\alpha & 0 & -l \\ 0 & -l\cos\alpha & 0 & l\cos\alpha & 0 & 0 \\ 0 & 1 & 0 & 1 & 0 & 1 \end{bmatrix} \tag{8}$$

Due to the sinusoidal variation of the magnetic-flux density in one direction on the horizontal plane of the linear Halbach array, the total Lorentz-force vector produced by the planar Lorentz actuators, each with either 3-phase coils [3,15] or 2-phase coils [24], is expressed as

$$\boldsymbol{F}_a = k\boldsymbol{S}\boldsymbol{i}, \tag{9}$$

where $\boldsymbol{i}$ is the coil current vector. Here, k is a constant depending on the peak magnetization of the magnets used to form the linear Halbach array, the array's spatial pitch and thickness, the coils' geometry, and the coil-magnet gap [3,15,24]. The constant k represents the actuator's force density for levitation and thrust. With the same actuator structure and magnet-coil gap, in this analysis the same constant k is assumed for all three designs in Figs. 6–8. The $\boldsymbol{S}$ matrix represents the position-dependent components of the current-force transformation. For the square and cross designs, $\boldsymbol{S}$ is a 8×8 matrix and $\boldsymbol{i}$ is a 8×1 vector. For the triangular designs $\boldsymbol{S}$ is 6×6 and $\boldsymbol{i}$ is 6×1. The derivations of k and $\boldsymbol{S}$ for a triangular design and a cross one can be found in Chapter IV of [26] and Chapter III of [27], respectively. The matrix $\boldsymbol{S}$ is formed by blocks of 2×2 rotational-transformation matrices in its diagonal. $\boldsymbol{S}$ is, therefore, orthogonal ($\boldsymbol{S}^{-1} = \boldsymbol{S}^{\boldsymbol{T}}$). This is the key advantage of the Lorentz-force actuators using a Halbach array. This allows for the currents to be calculated from the control efforts of the stage's controller without computing $\boldsymbol{S}^{-1}$ in real time.

To derive a linear model for the 6-DOF planar stage, Eq. (5) and $\boldsymbol{B}$, the pseudoinverse of the constant-element matrix $\boldsymbol{A}$, are used. The control effort vector, $\boldsymbol{U}$, is introduced by $\boldsymbol{F_a} = k\boldsymbol{BU}$, where $\boldsymbol{U} = [u_x\ u_y\ u_{\theta z}\ u_{\theta x}\ u_{\theta y}\ u_z]^T$. Each element of $\boldsymbol{U}$ is the decoupled control effort in one axis of the stage. Substituting $\boldsymbol{F_a} = k\boldsymbol{BU}$ into $\boldsymbol{F_t} = \boldsymbol{AF_a}$ yields $\boldsymbol{F_t} = k\boldsymbol{U}$. From this and $\boldsymbol{F_t} = \boldsymbol{M}\ddot{\boldsymbol{p}}$ (pure-mass model assumed), where $\boldsymbol{M}$ is the 6×6 mass matrix and $\boldsymbol{p}$ is the 6×1 position vector of the mover, the system model is formed as $\boldsymbol{M}\ddot{\boldsymbol{p}} = k\boldsymbol{U}$.

With $\boldsymbol{C}(s)$ being the 6×1 vector of decoupled controllers in 6 axes, one has $\boldsymbol{U}(s) = \boldsymbol{C}(s)\boldsymbol{E}(s)$, where $\boldsymbol{E}(s)$ represents the Laplace transform of the position-feedback error $\boldsymbol{e}(t)$. The control efforts in $\boldsymbol{U}$ are calculated based on the implemented feedback-controller structure. The coil currents are calculated based on Eq. (9) and $\boldsymbol{F_a} = k\boldsymbol{BU}$. This gives

$$\boldsymbol{i} = \boldsymbol{S}^T\boldsymbol{B}\boldsymbol{U}. \tag{10}$$

Because $\boldsymbol{S^T}$ is orthogonal, we have $||S^TB||_2 = ||B||_2$. Therefore, $||B||_2$ represents the magnitude of the current vector $\boldsymbol{i}$ depending on the control effort vector $\boldsymbol{U}$. In practice, when a cross-axis error force or torque occurs, the corresponding elements of the $\boldsymbol{A}$ matrix in Eq. (6–8) should be changed to reflect the error. With the cross-axis error forces, the accordingly-varied $\boldsymbol{B}$ should be the one that yields the accurate values of the coil currents to guarantee the desired performance of the designed controllers. However, practically only the constant-element (and nominal) $\boldsymbol{B}$ is used in real-time control. Therefore, there is an error between the calculated current vector (from the fixed $\boldsymbol{B}$) and the desired current vector that should be computed by the varied $\boldsymbol{B}$. With the same cross-axis error-force bound, it is, therefore, worth to estimate the variation range of $||\boldsymbol{B}||_2$ so that the variation of the magnitude of the coil current vector can be evaluated. Specifically, the envelope of $||\boldsymbol{B}_{varied}||_2/||\boldsymbol{B}_{nominal}||_2$ should be compared among the designs.

3.2.2. *Cross-axis coupling analysis for out-of-plane dynamics*

Assuming that the motor 1 generating a force F_{1x} in x has an error force in z of $\Delta F_z = \varepsilon_{1xz}F_{1x}$, where $|\varepsilon_{1xz}|$ is bounded by ε, the matrices of $\boldsymbol{A}$ as in Eq. (6–8) are changed as follows.

$$\boldsymbol{A}_{square\_varried} = \begin{bmatrix} 1 & 0 & 0 & 0 & 1 & 0 & 0 & 0 \\ 0 & 0 & 1 & 0 & 0 & 0 & 1 & 0 \\ -l & 0 & -l & 0 & l & 0 & l & 0 \\ -\varepsilon_{1xz}l & -l & \varepsilon_{2yz}l & l & \varepsilon_{3xz}l & l & -\varepsilon_{4yz}l & -l \\ -\varepsilon_{1xz}l & -l & -\varepsilon_{2yz}l & -l & \varepsilon_{3xz}l & l & \varepsilon_{4yz}l & l \\ \varepsilon_{1xz} & 1 & \varepsilon_{2yz} & 1 & \varepsilon_{3xz} & 1 & \varepsilon_{4yz} & 1 \end{bmatrix} \tag{11}$$

$$\boldsymbol{A}_{cross\_varied} = \begin{bmatrix} 0 & 0 & 1 & 0 & 0 & 0 & 1 & 0 \\ 1 & 0 & 0 & 0 & 1 & 0 & 0 & 0 \\ l & 0 & -l & 0 & -l & 0 & l & 0 \\ 0 & 0 & \varepsilon_{2xz}l & l & 0 & 0 & -\varepsilon_{4xz}l & -l \\ -\varepsilon_{1yz}l & -l & 0 & 0 & \varepsilon_{3yz}l & l & 0 & 0 \\ \varepsilon_{1yz} & 1 & \varepsilon_{2xz} & 1 & \varepsilon_{3yz} & 1 & \varepsilon_{4xz} & 1 \end{bmatrix} \tag{12}$$

$$\boldsymbol{A}_{tr\_varied} = \begin{bmatrix} -\sin\alpha & 0 & -\sin\alpha & 0 & 1 & 0 \\ \cos\alpha & 0 & -\cos\alpha & 0 & 0 & 0 \\ l & 0 & l & 0 & l & 0 \\ \varepsilon_{1hz}l\sin\alpha & l\sin\alpha & \varepsilon_{1hz}l\sin\alpha & l\sin\alpha & -\varepsilon_{3hz}l & -l \\ -\varepsilon_{1hz}l\cos\alpha & -l\cos\alpha & \varepsilon_{2hz}l\cos\alpha & l\cos\alpha & 0 & 0 \\ \varepsilon_{1hz} & 1 & \varepsilon_{2hz} & 1 & \varepsilon_{3hz} & 1 \end{bmatrix} \tag{13}$$

It is noticed that $1/||\boldsymbol{B}||_2$ is the lower bound of $||\boldsymbol{A}||_2$, and, therefore, is a continuous function on the open set of the matrix elements [28]. Given the fact that ε_{juv} varies in $[-\varepsilon, \varepsilon]$, this discussion is not aimed at deriving a rigorous analysis to constrain $||\boldsymbol{B}||_2$ but providing an estimate of the envelope of the ratio between the 2-norm of the varied $\boldsymbol{B}$ (calculated from the varied $\boldsymbol{A}$ in Eq. (11–13)), and that of the nominal $\boldsymbol{B}$ (from the nominal $\boldsymbol{A}$ in Eq. (6–8)). This is accomplished by computing the ratio of $||\boldsymbol{B}_{varied}||_2/||\boldsymbol{B}_{nominal}||_2$ with all the elements of ε_{juv} switched between evenly distributed values in $[-\varepsilon, \varepsilon]$. With $l = 0.1$ m and $\varepsilon \in [0.01, 0.22]$, the envelopes of this ratio for all three designs are plotted in Fig. 9. It is seen that the triangular configuration has the narrowest envelope and the square configuration has the largest one.

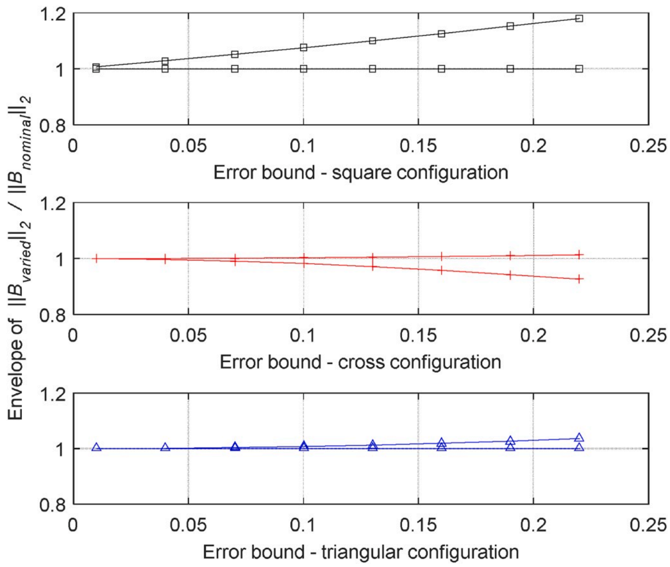

Fig. 9. The envelope of $||\boldsymbol{B}_{varied}||_2/||\boldsymbol{B}_{nominal}||_2$ for the out-of-plane dynamics.

3.2.3. Force-error analysis for in-plane dynamics

The force error considered here is the difference between the actual force generated by an actuator and the desired force to be generated in the same axis at the same time. The force error herein can be a static or dynamic one. The static force error is due to the coil fill factor, the actuator's geometrical errors, and errors in the PMs' magnetizations. The causes of the dynamic errors, which mainly occur in the transient responses of the system, include actuator saturation, current-amplitude errors, and currents' phase lag. This lag is due to not only the slew rate but also the phase change in the power-electronic dynamics at high frequencies. In addition, the dynamic errors in the actuators' forces during transient motions can be caused by the error angle between the moving platen and the stationary array of magnets or coils (the force calculation is made with the assumption that the magnet and coil arrays are perfectly aligned). The force errors in the stage's in-plane dynamics become dominant when the mover performs high-acceleration motions, or is subject to a large and off-center load, an impact, or strong vibrations.

For the in-plane dynamics of x, y, and the rotation about the vertical axis, the corresponding $\boldsymbol{A}$ matrix can be reduced from Eq. (11–13).

$$\boldsymbol{A}_{square\_inplane} = \begin{bmatrix} 1 & 0 & 1 & 0 \\ 0 & 1 & 0 & 1 \\ -l & -l & l & l \end{bmatrix} \tag{14}$$

$$\boldsymbol{A}_{cross\_inplane} = \begin{bmatrix} 0 & 1 & 0 & 1 \\ 1 & 0 & 1 & 0 \\ l & -l & -l & l \end{bmatrix} \tag{15}$$

$$\boldsymbol{A}_{tr\_inplane} = \begin{bmatrix} -\sin\alpha & -\sin\alpha & 1 \\ \cos\alpha & -\cos\alpha & 0 \\ l & l & l \end{bmatrix} \tag{16}$$

We consider the case when each Lorentz force component in XY has a force error, where the actual force component is $F_{1x}(1+\varepsilon_{1x})$. Here F_{1x} is the desired Lorentz force to be generated by actuator 1 in x, and $|\varepsilon_{1x}|$ is bounded by ε. The forces generated by the actuators are combined to drive the moving platen in one axis and minimize the position fluctuations in the other axes, all in closed-loop control. A force error at one actuator, therefore, requires other actuators to respond accordingly to compensate for this error. The $\boldsymbol{A}$ matrices with the force errors in x and y for the three design configurations mentioned above are

$$\boldsymbol{A}_{square\_varied} = \begin{bmatrix} 1+\varepsilon_{1x} & 0 & 1+\varepsilon_{3x} & 0 \\ 0 & 1+\varepsilon_{2y} & 0 & 1+\varepsilon_{4y} \\ -l(1+\varepsilon_{1x}) & -l(1+\varepsilon_{2y}) & l(1+\varepsilon_{3x}) & l(1+\varepsilon_{4y}) \end{bmatrix}, \tag{17}$$

$$\boldsymbol{A}_{cross\_varied} = \begin{bmatrix} 0 & 1+\varepsilon_{2x} & 0 & 1+\varepsilon_{4x} \\ 1+\varepsilon_{1y} & 0 & 1+\varepsilon_{3y} & 0 \\ l(1+\varepsilon_{1y}) & -l(1+\varepsilon_{2x}) & -l(1+\varepsilon_{3y}) & l(1+\varepsilon_{4x}) \end{bmatrix}, \tag{18}$$

$$\boldsymbol{A}_{tr\_varied} = \begin{bmatrix} -(1+\varepsilon_{1h})\sin\alpha & -(1+\varepsilon_{2h})\sin\alpha & 1+\varepsilon_{3h} \\ (1+\varepsilon_{1h})\cos\alpha & -(1+\varepsilon_{2h})\cos\alpha & 0 \\ l(1+\varepsilon_{1h}) & l(1+\varepsilon_{2h}) & l(1+\varepsilon_{3h}) \end{bmatrix}. \tag{19}$$

Fig. 10 gives the envelopes of $||\boldsymbol{B}||_2$ for the $\boldsymbol{A}$ matrices in Eq. (17–19) in case one actuator of the associated system has a bounded force error specified by $\varepsilon \in [0.01, 0.22]$. For the in-plane dynamics, the envelopes for the square and cross designs are the same and smaller than that of the triangular one. This indicates that the effect of the actuators' force errors on the triangular design is worse than that on the square and cross ones.

In case a 6-DOF vibration-isolation stage is of interest (no need for high-speed motions in XY), this analysis suggests that the triangular one is the choice. If a long-stroke and high-speed stage is needed, where a compact mover is required and the out-of-plane dynamics is not a concern, the square design is the selection. If a long-stroke and high-speed stage is needed, where the mover is magnetically levitated by Lorentz forces, the cross design helps reduce the effects of the off-axis error forces on the out-of-plane dynamics and the XY force errors on the in-plane dynamics.

3.3. The cross-coupling quantity

The objective of proposing the CCQ in this paper is to introduce, for the first time, a quantity that represents the degree of cross-axis couplings in the transient responses of multi-axis stages. The reported works in the literature were all with different command profiles, leaving a challenge for comparing the levels of cross-axis couplings in the stages [4,16,17,27]. There may not be a unique measure that can be universally used for all the cases. Depending on the priority in particular applications, one may put another weighing factor in the CCQ formula for the comparisons. Here, we introduce a simple CCQ formula and our experimental results as a benchmark so that, based on this, further studies and comparisons will be conducted for other stage configurations tailored for specific applications.

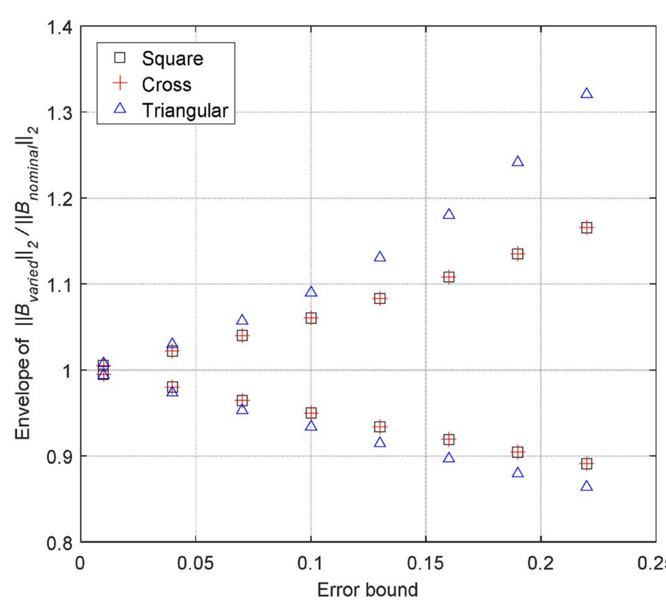

Fig. 10. The envelope of $||\boldsymbol{B}_{varied}||_2/||\boldsymbol{B}_{nominal}||_2$ for the in-plane dynamics.

The CCQ is defined for each pair of a primary axis and a perturbed axis and calculated as the product of the transient response's peak time in the primary axis and the ratio between the p-p fluctuation in the perturbed axis and the primary axis' displacement. The CCQ between the perturbed axis of θ_z and the primary axis of θ_y is $t_p\theta_{z\_pp}/\theta_{y\_d}$, where t_p and θ_{y_d} are, respectively, the peak time of the response and the displacement along θ_y. The p-p position fluctuation in θ_z is θ_{z_pp}.

The peak time is used to calculate the CCQ for three reasons. First, it takes into account the speed and acceleration of the primary axis' motion. Second, the duration of the peak time is the window when the peak fluctuation in the perturbed axis is most likely to occur. Third, for a given plot of a response, the peak time can be estimated without the need of the raw data. The p-p perturbations, not rms position errors, are of interest because a large p-p position fluctuation in an interferometer stage may cause laser-signal loss, catastrophic instability, and maglev-mover touch down. This is critical for air-bearing and maglev stages because there is no mechanical surface to constrain the mover along the perturbed axes. The peak time or rise time in the perturbed axis is not included because these quantities are only well defined in the step responses along the primary axis. For maglev and air-bearing stages with a single moving part, the transient responses from which the CCQ are calculated are in closed-loop control.

The unit of a CCQ depends on the type of motions, translational or rotational, in the primary and the perturbed axes. Table 3 provides the CCQ units in all possible combinations. A decrease in the CCQ implies a reduction and, therefore, an improvement in the cross-axis coupling.

4. Experimental validation

4.1. Design and fabrication of a cross-configuration 6-DOF maglev stage

This part presents the design and fabrication of the moving platen of a cross-configuration moving-coil maglev stage. Its stationary part, a superimposed magnet matrix over which the single moving part developed herein moves, was previously constructed [15] and utilized [24].

Together with the cross configuration, a key feature that helps reduce the cross-axis couplings is the overlapped Lorentz coils to increase the force density and reduce the spatial variations of the acting points of the equivalent vertical forces. In this design, a Lorentz forcer is a set of two Lorentz coils with one side of each coil placed in the space between the two sides of the other coil. The four sides of two coils are, therefore, evenly placed with a spacing of a quarter of the linear Halbach array's pitch. The coils' short sides, which are not effective for force generation, are bent and curved to be further away from the magnets' surface. A tooling fixture was designed exclusively for the overlapped coils with the curved coil ends, as shown in Fig. 11. The copper wire used to make the coils is AWG 20 bondable magnet wire. A set of two overlapped coils weighs 51.3 g. The resistance and inductance of each coil are 0.19 Ω and 59 μH, respectively. The thickness of the coils is 2.54 mm, and the width of the coil sides is 9.65 mm. The effective length for Lorentz force generation of each side is 42.29 mm.

The cross configuration's layout with the above-mentioned overlapped coils and the 2-D Halbach matrix are depicted in Fig. 12. The magnetic field of the 2-D Halbach matrix formed by the superimposition of two single-axis linear Halbach arrays is illustrated in Fig. 13. Each pair of two overlapped coils with the sides along the x-axis generates two independent Lorentz forces, one in y and the other in z. Only the y and z flux-density components, which are sinusoidally varying in y and illustrated in the top left corner of Fig. 13, contribute to these Lorentz forces.

Table 3
The CCQ units in all the combinations (T: translational, R: rotational)

Primary axis	T	T	R	R
Perturbed axis	T	R	T	R
CCQ	s	rad·s/m	m·s/rad	s

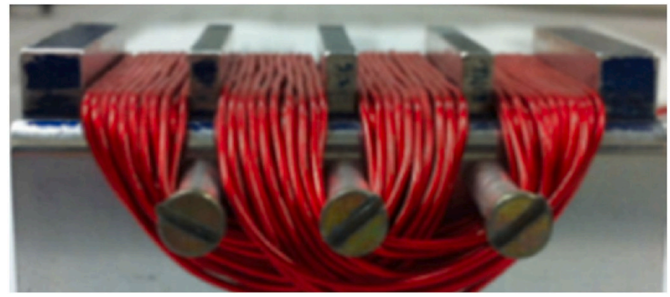

Fig. 11. An overlapped pair of coils wound in the tooling fixture.

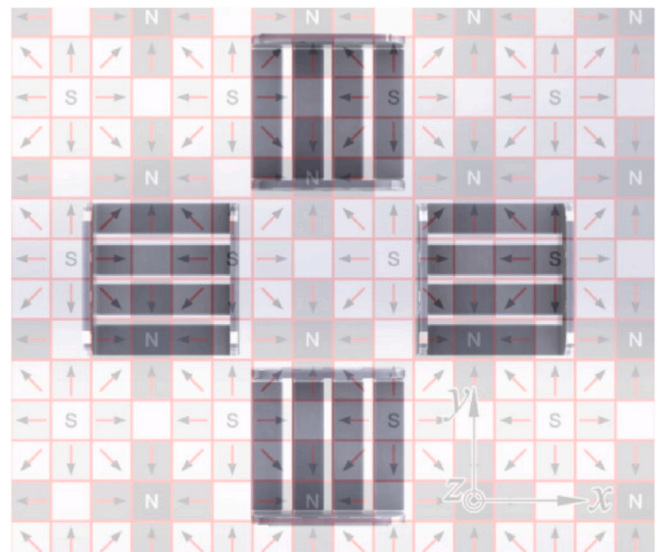

Fig. 12. The cross design with 4 pairs of coils working with a 2-D Halbach magnet matrix.

With the same coil pair having the sides along x, the flux density components that vary sinusoidally in x (bottom left corner of Fig. 13) produce net-zero Lorentz forces in y and z. This significantly simplifies the force model of the system because only the field solution for one linear Habach array, not the superimposed field of the magnet matrix, is used to compute the Lorentz force for each set of two coils. The use of the superimposed magnet matrix allows for a compact size of the overall structure relative to the travel range of the mover. The ratio between the maximum possible stroke in XY of the stage developed in this work and the size of its stationary magnet matrix is 0.50. The multi-axis stage with separated single-axis Halbach arrays reported in Ref. [2] had the load capability considerably larger than that of our stage presented in this paper. However, for the design in Ref. [2], the ratio between the maximum stroke in XY and the overall size of the stationary coil array was only 0.02.

The assembly of the four coil pairs and the moving platen's frame is depicted in Fig. 14. A photograph of the fully assembled moving part is given in Fig. 2. The size of the square platen's frame is 142.5 mm × 142.5 mm, and the thickness of the moving part without the vertical-displacement laser sensors is 18.0 mm. The total mass of the stage's single moving part is 0.750 kg and that of all 8 copper coils is 0.205 kg. After the assembly to the moving platen's frame, the flat surfaces of the 4 coil sets (one set is shown in Fig. 11) are aligned to form the bottom surface of the moving part. The nominal distance between this bottom surface of the moving part and the top surface of the magnet matrix is used in the derivation of the Lorentz forces [27]. The spatial pitch in each side, x and y, of the planar Halbach matrix used in this work is 50.8

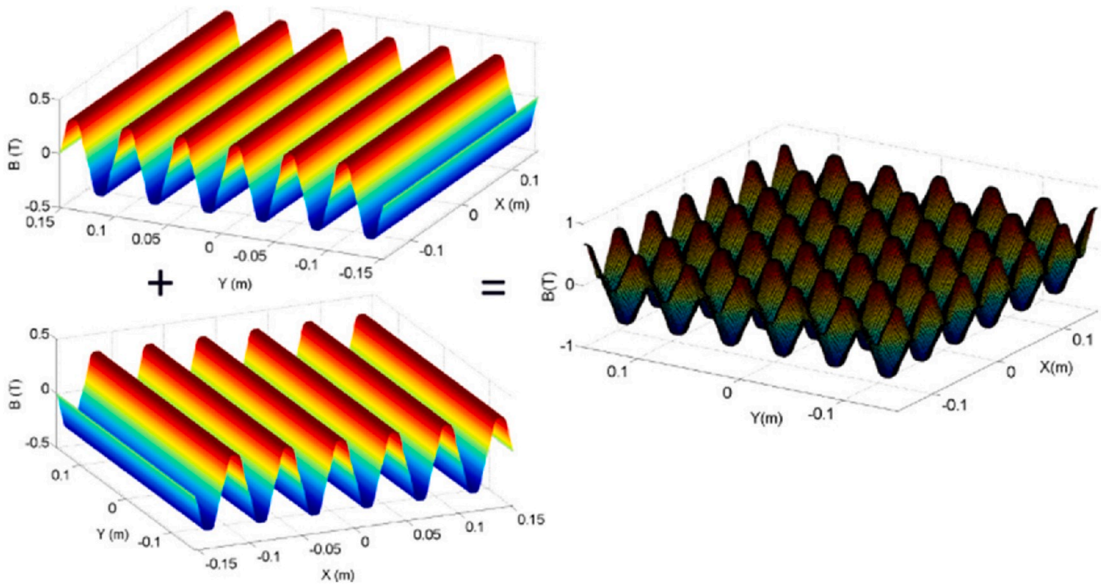

Fig. 13. Illustration of the superimposition of two single-axis linear Halbach arrays to form a superimposed Halbach magnet matrix.

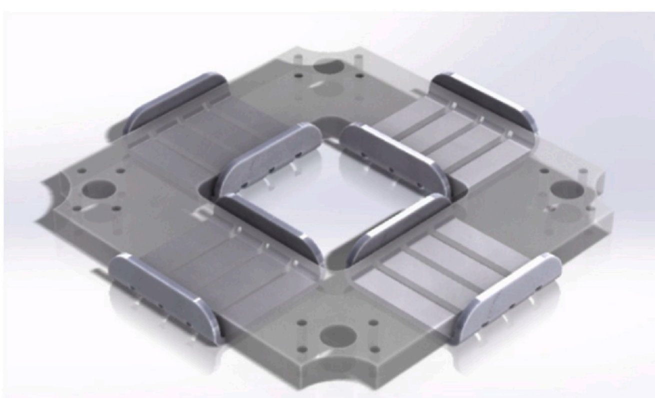

Fig. 14. A 3-D rendering of the overlapped Lorentz coils attached to the moving part.

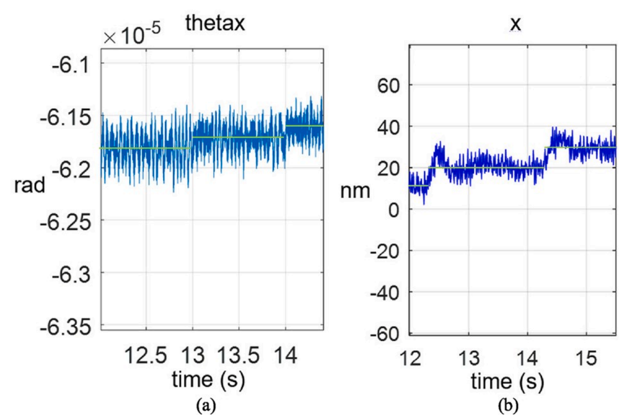

Fig. 15. Minimum step sizes in (a) out-of-plane rotation and (b) in-plane translation.

mm. The spacing between two nearby coil sides shown in Fig. 11 is 12.7 mm.

4.2. Multi-axis positioning performance

The system modeling and proportional-integral-derivative (PID) controller design for this 6-DOF maglev stage can be found in Ref. [27]. Fig. 15(a) demonstrates two consecutive steps of 0.1 μrad in θ_x, the rotation about the x-axis as seen in Fig. 7. This is a record in the literature of 6-axis nanopositioning, indicating how quiet the motion system is. The average p-p positioning noise is 0.6 μrad and the achieved rms position noise is 0.1 μrad. Fig. 15(b) is the plot of two 10-nm steps in the x-axis. The rms position noise here is 3 nm. This is unprecedented for a 6-DOF motion system with a single moving part and the XY strokes on the order of centimeters.

Fig. 16 includes a step response of 1.5 μm in θ_y and the perturbations in all other 5 axes. Although being useful in showing the effects of cross-axis couplings in multi-axis positioning, results of this type were rarely found in the prior works on multi-DOF motion system design. The position fluctuations in other axes are within 60 nm in x, 20 nm in y, 0.4 μrad in θ_z, and 40 nm in z, respectively. Table 4 shows the CCQ values between the perturbed axes and the primary axis of θ_y in the 1.5-μm step seen in Fig. 16. The CCQ between θ_x and θ_y in this case is negligibly small.

Fig. 17 presents two consecutive step responses in the primary axis of θ_x and the associated perturbations in the other 5 axes. It is seen that the perturbations caused by the second step of 148 μrad in the primary axis are larger than those resulted from the first 148-μrad step. The reason is that the second step is performed in only 0.25 s after the first step is settled (at 13 s) in the primary axis. At 13.25 s the fluctuations in other axes caused by the first step of 148 μrad in θ_x are not completely attenuated. Table 5 contains the CCQ values between θ_x and the other axes in the two motion profiles in Fig. 17. The peak time of each response is 1.0 s.

Fig. 18 shows two consecutive step responses of 2 μrad and −4 μrad in θ_z and the perturbations in the other five axes. In this case, the position fluctuations in the perturbed axes caused by the first step response in the primary axis already settles down before the second step in θ_z is performed. In all of the perturbed axes, except for x, the p-p perturbations due to the second step are larger than those of the first step. This is consistent with the fact that the step size along the primary axis in the second step is twice that of the first step. Table 6 provides the CCQ values between θ_z and the other axes in the two motion profiles seen in Fig. 18. The peak time of each response is 0.3 s.

The two consecutive responses in Fig. 18 are further separated in time compared to those in Fig. 17. For the perturbations in Fig. 18, three

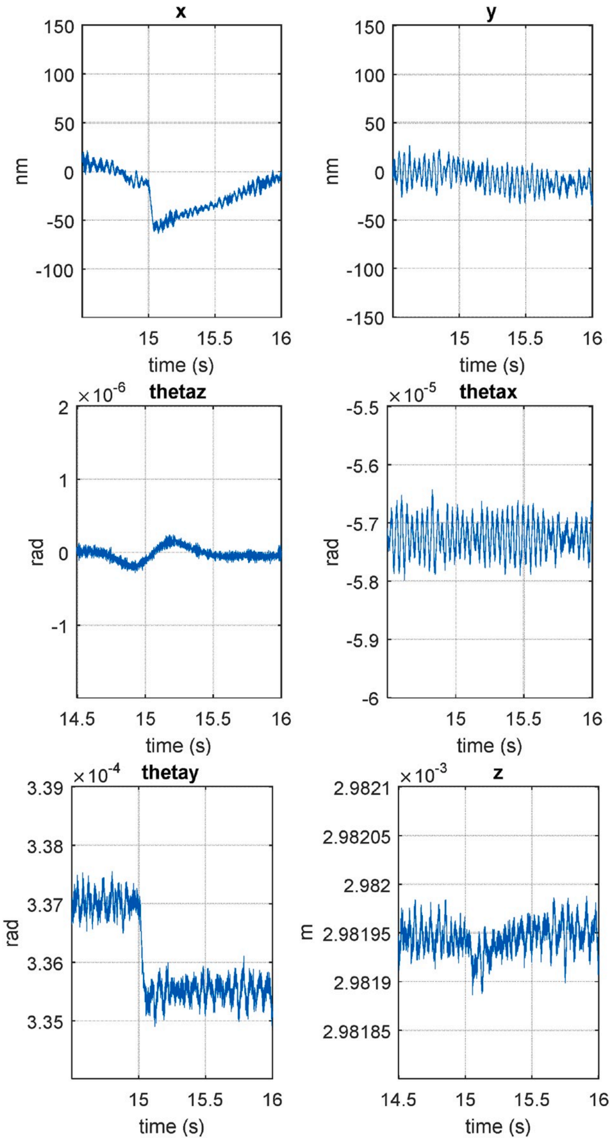

Fig. 16. A 1.5-μrad step motion in θ_y and perturbations in other axes.

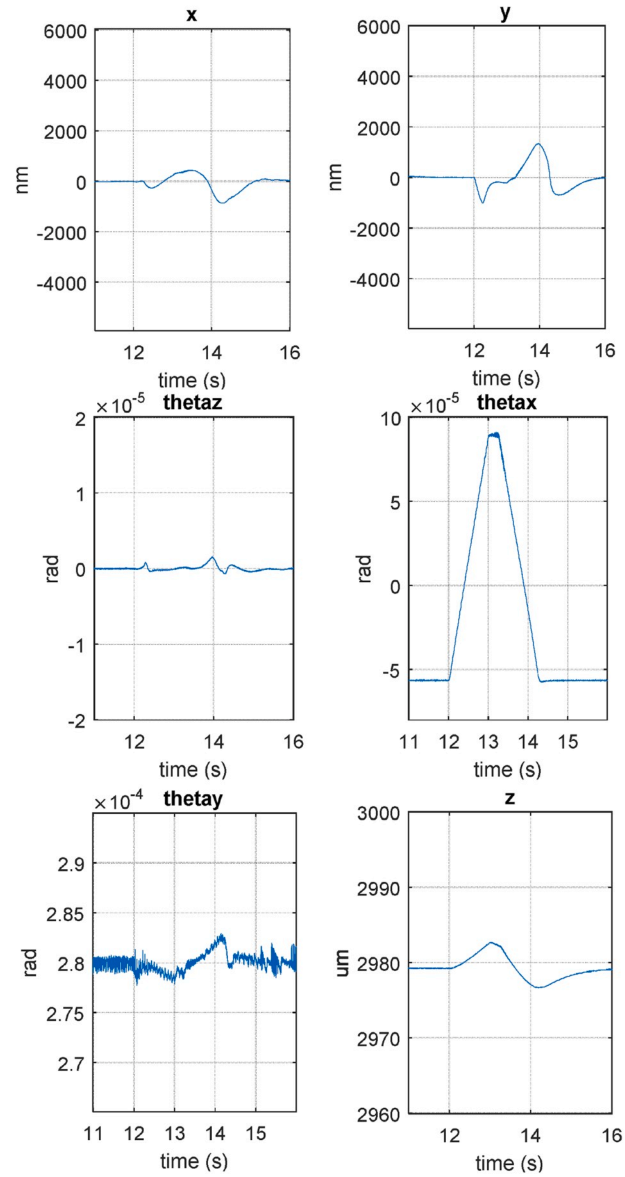

Fig. 17. A trapezoidal position profile of 148-μrad in θ_x and perturbations in other axes.

Table 4
The CCQ values between θ_y and other axes in the 1.5-μrad step presented in Fig. 16.

Axis	x	y	θ_z	θ_x	z
CCQ	0.0020	0.0005	0.0117	Negligible	0.0013
Unit	m·s/rad	m·s/rad	s	s	m·s/rad

of the CCQ values in the first and the second motion profiles are the same. This result suggests that in stepping motions of multi-axis maglev or air-bearing stages with a single moving part, the transient responses must be sufficiently separated in time so that the fluctuations in the first step can be attenuated before the second step is performed.

Fig. 19 demonstrates a response with the step size of 2 μm in y and the position perturbations along the in-plane axes of x and θ_z. The peak time of the step response in y is 0.05 s. Table 7 lists the CCQ values between y and the other axes, x and θ_z.

Fig. 20 plots a transient response with the displacement of 14 mm in x and the position perturbations along the in-plane axes of y and θ_z. The peak time of this position profile is 0.30 s. Table 8 gives the CCQ values between x and the other axes, y and θ_z.

Only for the long-range motions of 148 μrad in θ_x and 14 mm in x reported in Figs. 17 and 20, respectively, command shaping with a trapezoidal velocity profile was used to make the motion smooth, reducing position fluctuations in the primary axis and perturbations in the other axes. Comparing the response in Fig. 16 (1.5 μrad in θ_y for 0.05 s) with the first one in Fig. 17 (148 μrad in θ_x for 1 s), the trapezoidal-velocity command shaping helps make two of the CCQ values

Table 5
The CCQ values between θ_x and other axes in the rotations of 148 μrad in Fig. 17.

Axis	x (nm)	y (nm)	θ_z (μrad)	θ_y (μrad)	z (μm)
1st step's p-p perturbation	285	1015	1.20	1.50	3.45
2nd step's p-p perturbation	1301	2037	2.24	3.00	5.49
CCQ (1st step)	0.0019	0.0069	0.0081	0.0101	0.0233
CCQ (2nd step)	0.0088	0.0138	0.0151	0.0203	0.0371
CCQ unit	m·s/rad	m·s/rad	s	s	m·s/rad

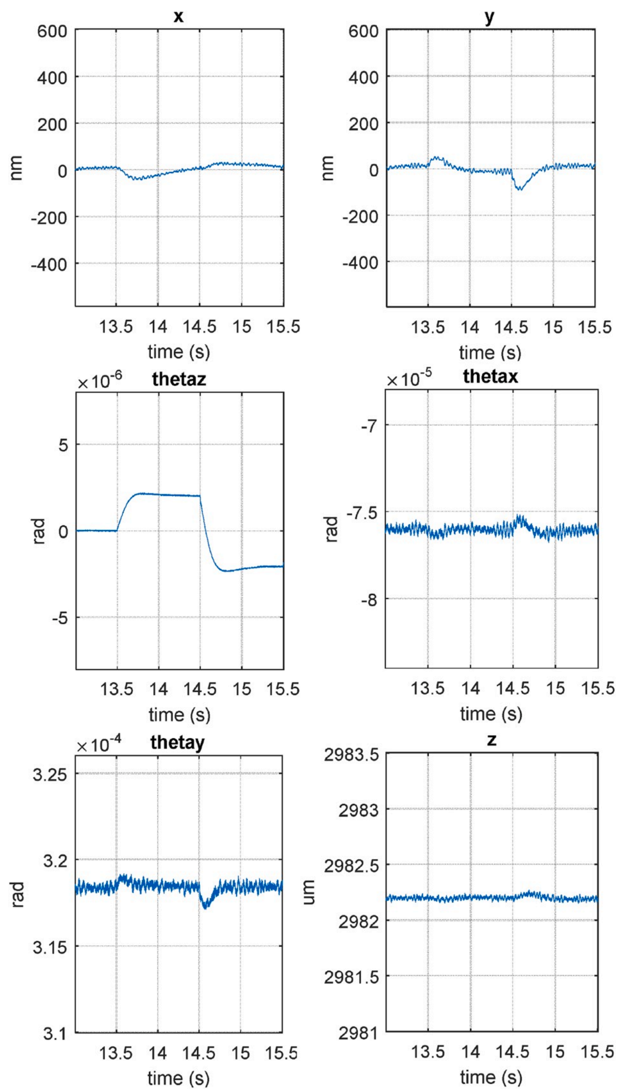

Fig. 18. Two steps, 2 and −4 μrad, in θ_z and perturbations in other axes.

Table 6
The CCQ values between θ_z and other axes in the steps of 2 μrad and −4 μrad in Fig. 18.

Axis	x (nm)	y (nm)	θ_x (μrad)	θ_y (μrad)	z (μm)
1st step's p-p perturbation	50	37	0.40	0.50	0.02
2nd step's p-p perturbation	17	74	0.80	1.00	0.06
CCQ (1st step)	0.0075	0.0056	0.0600	0.0750	0.0030
CCQ (2nd step)	0.0013	0.0056	0.0600	0.0750	0.0045
CCQ unit	m·s/rad	m·s/rad	s	s	m·s/rad

(between x, θ_z, and the primary axis) for the 148-μrad profile better than those of the 1.5-μrad one. It is noticed that the average velocity in the 148-μrad response is approximately 5 times that of the 1.5-μrad displacement.

The CCQ values presented in Fig. 20 are significantly better than those shown in Fig. 19 although the former, performed with trapezoidal-velocity command shaping, has a step size of 14 mm, which is 7000 times larger than that of the later. Their peak times are different by a factor of 6. This clearly demonstrates the positive effect of command shaping to reduce position errors in the transient responses of the motion

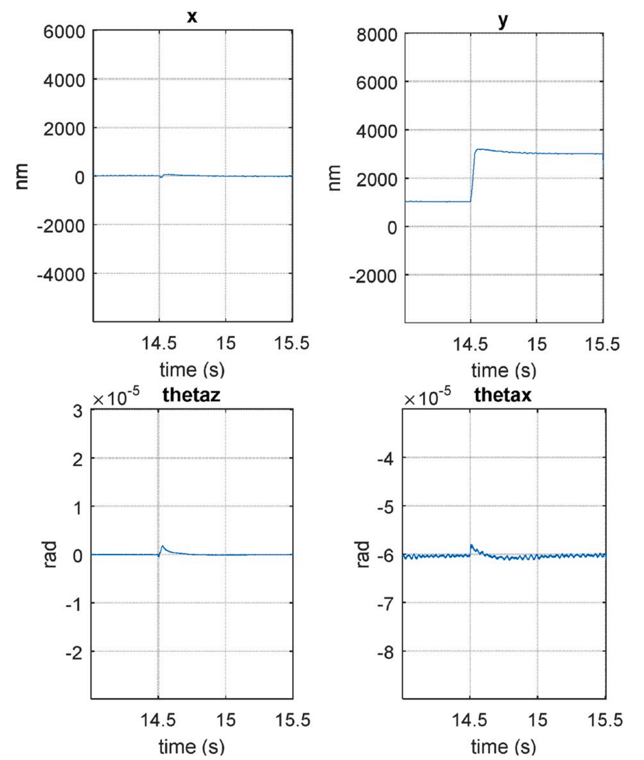

Fig. 19. A step motion of 2 μm in y and perturbations in x and θ_z.

Table 7
The CCQ values between y and other axes in the 2.0-μm step response in Fig. 19.

Axis	x (nm)	θ_z (μrad)	θ_y (μrad)
p-p perturbation	127	2.3	3.0
CCQ	0.0032	0.0575	0.0750
CCQ unit	s	rad·s/m	rad·s/m

stage. The perturbed fluctuation in y is provided in Fig. 21.

4.3. *Comparisons with existing experimental results in multi-axis positioning*

Fig. 14 of [16] reports a step response of 7 mm in x and y with the peak time of 0.1s, the p-p perturbations are 9.5 mrad in θ_z, and 4 mrad in θ_y. Compared with the CCQ of our 6-DOF maglev stage in Table 8, the CCQ between the primary axis and the out-of-plane rotation in Ref. [16] is 2.8 times larger, and that between the primary axis and the in-plane rotation in Ref. [16] is 46.8 times larger, as seen in Table 9. The design configuration in Ref. [16] is a triangular one. The effect of cross-axis couplings on the in-plane dynamics of this triangular stage is of a significantly greater concern compared to that of our cross-configuration design. This is consistent with our analysis in Section 3 of this paper.

Fig. 16(c) of [4] presents a translational motion of 30 mm in y, the primary axis. The rms position error in x is 8.6 μm, and the peak time in y is approximately 0.3 s. The CCQ between y and x is 90 μs. In our experimental result shown in Figs. 20 and 21, the rms position error in y is 2.4 μm, and the CCQ calculated from this response is 50 μs. Our result demonstrates the advantage of reducing the number of coils and using longer coils with better straightness to minimize the couplings.

5. Conclusions

The problem of cross-axis couplings is dominant in precision multi-axis positioning. For motion stages with mechanical bearings, the cross-

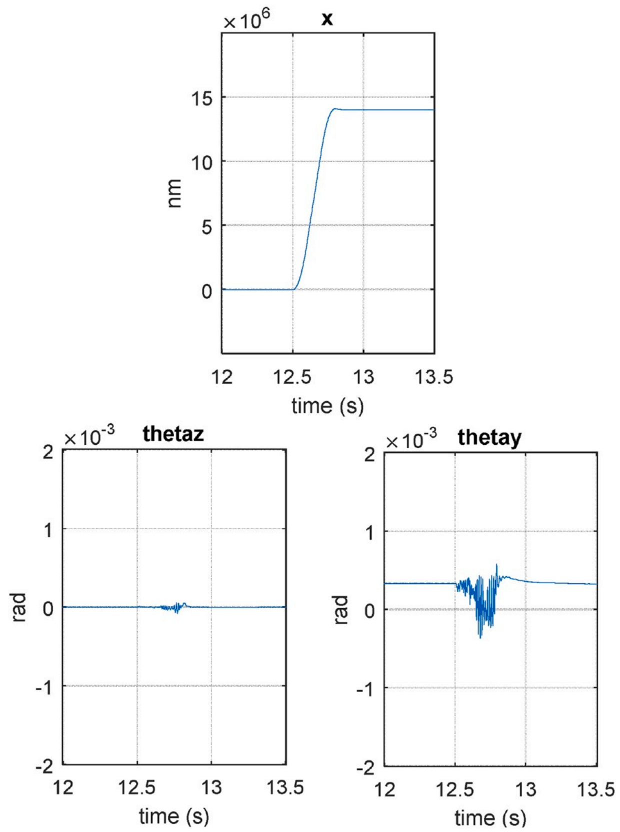

Fig. 20. A step motion of 14 mm in x and perturbations in θ_z and θ_y.

Table 8
The CCQ values between x and other axes in the 14-mm step response in Fig. 20.

Axis	y (μm)	θ_z (μrad)	θ_y (μrad)
p-p perturbation	16.5	134.8	945
CCQ	0.0004	0.0029	0.0203
CCQ unit	s	rad·s/m	rad·s/m

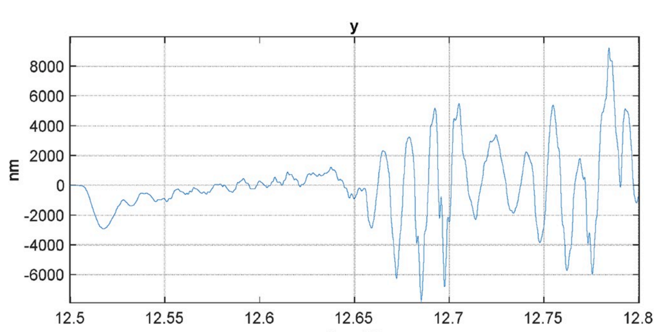

Fig. 21. The perturbations in y of the translation in x shown in Fig. 20.

Table 9
The CCQ values between x and two rotational axes, one in-plane and the other one out-of-plane in the 7-mm step response of [16].

Axis	θ_z (mrad)	θ_y (mrad)
p-p perturbation	9.5	4.0
CCQ	0.1357	0.0571
CCQ unit	rad·s/m	rad·s/m

axis couplings may not produce significant position perturbations in all axes. However, it still causes undesired force disturbances to the control systems. For maglev and air-bearing stages, cross-axis couplings lead to perturbed position errors in all the axes and possibly instability due to the loss of the position-measurement signals. Static parasitic errors in precision positioning have been addressed in the literature. However, these errors were discussed only for positioning with flexure stages or multi-moving-part stages with mechanical bearings, in which the flexure structures and mechanical bearings' imperfections were the main causes of parasitic errors. For maglev and air-bearing stages, the perturbed position errors (or cross-axis perturbations) are caused by both in-axis and off-axis errors in the forces. This occurs statically due to the stages' geometrical errors and dynamically due to many reasons including the power electronics' dynamics, the position-dependent end-effects of magnets and coils, and misalignments between the mover and stationary part during transient responses. For maglev and air-bearing stages the errors occurred dynamically are more of a concern compared to the static errors because the dynamic errors may remain hidden at low speed. Means to quantify and compare the effects of cross-axis couplings in transient responses did not exist.

This paper presents a detailed analysis on the maps between the bounded errors of the actuators' forces and the variation ranges of the coil currents in closed-loop control for three stage design configurations—triangular, cross, and square. Our analysis indicates that the cross-configuration is with the highest potential of minimizing the cross-axis couplings in 6-DOF planar stages with long strokes. This analysis is supported by the experimental results obtained from our 6-axis maglev stage with 8 Lorentz coils and a Halbach magnet matrix. With the total weight of the coils of only 0.205 kg, the achieved translational-motion speed and acceleration are 70 mm/s and 1.4 m/s^2, respectively. Comparisons with the performances of previously-reported multiaxis stages show that our stage offers significantly reduced cross-axis perturbations during a mm-scale translational motion. In addition, the CCQ is defined in this paper to be used as a key measure in the comparisons between the performances of multiaxis positioning systems. Five sets of experimental results with the corresponding CCQ values are provided as a benchmark.

Appendix A. Supplementary data

Supplementary data to this article can be found online at https://doi.org/10.1016/j.precisioneng.2019.11.013.

References

[1] Verma S, Shakir H, Kim WJ. Novel electromagnetic actuation scheme for multi-axis nanopositioning. IEEE Trans Magn 2006;42(8):2052–62.
[2] Fesperman R, Ozturk O, Hocken R, Ruben S, Tsao TC, Phipps J, Lemmons T, Brien J, Caskey G. Multi-scale alignment and positioning system – maps. Precis Eng 2012;36(4):517–37.
[3] Compter IJC. Electro-dynamic planar motor. Precis Eng 2004;28:171–80.
[4] Zhu H, Teo TJ, Pang CK. Design and modeling of a six-degree-of-freedom magnetically levitated positioner using square coils and 1-D Halbach arrays. IEEE Trans Ind Electron 2017;64(1):440–50.
[5] Gorman JJ, Dagalakis NG, Boone BG. Multiloop control of a nanopositioning mechanism for ultraprecision beam steering. Proc SPIE, free-space laser communication and active laser illumination III. Jan. 2004. p. 5160.
[6] Kenton BJ, Leang KK. Design and control of a three-axis serial-kinematic high-bandwidth nanopositioner. IEEE/ASME Trans Mech 2012;17(2):356–69.
[7] Awtar S, Ustick J, Sen S. An XYZ parallel-kinematic flexure mechanism with geometrically decoupled degrees of freedom. J Mech Robot 2013;5:015001–7.
[8] Roy NK, Cullinan MA. Design and characterization of a two-axis, flexure-based nanopositioning stage with 50 mm travel and reduced higher order modes. Precis Eng 2018;53:236–47.
[9] Hicks TR, Atherton PD. The NanoPositioning Book. Queensgate Instruments Ltd; 1997.
[10] Smith ST, Seugling RM. Sensor and actuator considerations for precision, small machines. Precis Eng 2006;30(3):245–64.
[11] Schmidt RHM. Ultra-precision engineering in lithographic exposure equipment for the semiconductor industry. Phil Trans R Soc A 2012;370:3950–72.
[12] Deshmukh AA, Petit L, Khan MU, Lamarque F, Prelle C. A novel 3-D electromagnetic digital actuator with 12 discrete positions. IEEE/ASME Trans Mech 2018;23(4):1653–61.

[13] Cheng H, Chen H, Mooring BW. Accuracy analysis of dynamic-wafer-handling robotic system in semiconductor manufacturing. IEEE Trans Ind Electron 2014;61 (3):1402–10.
[14] Sreenivasan SV. Nanoimprint lithography steppers for volume fabrication of leading-edge semiconductor integrated circuits. Microsyst Nanoeng 2017;3:17075.
[15] Hu T, Kim WJ. Extended range six DOF high-precision positioner for wafer processing. IEEE/ASME Trans Mech 2006;11(6):682–9.
[16] Chen MY, Lin TB, Hung SK, Fu LC. Design and experiment of a macro–micro planar maglev positioning system. IEEE Trans Ind Electron 2012;59(11):4128–39.
[17] Basovich S, Arogeti SA, Menaker Y, Brand Z. Magnetically levitated six-DOF precision positioning stage with uncertain payload. IEEE/ASME Trans Mech 2016; 21(2):660–73.
[18] Jansen JW, Lierope VCMM, Lomonova EA, Vandenput AJA. Magnetically levitated planar actuator with moving magnets. IEEE Trans Ind Appl 2008;44(4):1108–15.
[19] Gu J, Kim WJ. Nanoscale motion control with a compact minimum-actuator magnetic levitator. J Dyn Syst Meas Control 2005;127:433–42.
[20] Freudenberg J, Middleton R, Stefanpoulou A. A survey of inherent design limitations. Proc Am Control Conf, Chicago, IL 2000;5:2987–3001.
[21] Heertjes M, Steinbuch M. Stability and performance of a variable gain controller with application to a dvd storage drive. Automatica 2004;40:591–602.
[22] Franklin GF, Powell JD, Emami-Naeini A. Feedback control of dynamic systems. In: Pearson education. seventh ed. 2015.
[23] Trumper DL, Williams ME, Nguyen TH. Magnet arrays for synchronous machines. Proc IEEE IAS 28th Annual Meeting Oct. 1993;1:9–18.
[24] Nguyen VH, Kim WJ. Design and control of a compact lightweight planar positioner moving over a concentrated-field magnet matrix. IEEE/ASME Trans Mech 2013;18(3):1090–9.
[25] Kim WJ. High-Precision Planar Magnetic Levitation. Ph.D. Dissertation. Cambridge, MA: Massachusetts institute of technology; Jun. 1997.
[26] Hu T. Design and control of a 6-Degree-of-Freedom levitated positioner with high precision. Ph.D. dissertation. College Station, TX: Texas A&M University; May 2005.
[27] Nguyen VH. Universal framework for linear motors and multi-Axis stages with magnetic levitation. Ph.D. dissertation. College Station, TX: Texas A&M University; Dec. 2015.
[28] Grcar JF. A matrix lower bound. Linear Algebra Appl 2010;433(1):203–20.